MR Contrast due to Intravascular Magnetic Susceptibility Perturbations

Jerrold L. Boxerman, Leena M. Hamberg, Bruce R. Rosen, Robert M. Weisskoff

A particularly powerful paradigm for functional MR imaging of microvascular hemodynamics incorporates paramagnetic materials that create significant image contrast. These include exogenous (lanthanide chelates) and endogenous (deoxygenated hemoglobin) agents for mapping cerebral blood volume and neuronal activity, respectively. Accurate interpretation of these maps requires an understanding of the biophysics of susceptibility-based image contrast. The authors developed a novel Monte Carlo model with which the authors quantified the relationship between microscopic tissue parameters, NMR imaging parameters, and susceptibility contrast *in vivo*. The authors found vascular permeability to water and the flow of erythrocytes to be relatively unimportant contributors to susceptibility-induced ΔR2. However, pulse sequence, echo time, and concentration of contrast agent have profound effects on the vessel size dependence of ΔR2. For a model vasculature containing both capillaries and venules, the authors predicted a linear volume fraction dependence for physiological volume changes based on recruitment and dilation, and a concentration dependence that is nonlinear and pulse sequence dependent. Using the model, the authors demonstrated that spin echo functional images have greater microvascular sensitivity than gradient echo images, and that the specifics of the volume fraction and concentration dependence of transverse relaxivity change should allow for robust mapping of relative blood volume. The authors also demonstrated excellent agreement between the predictions of their model and experimental data obtained from the serial injection of superparamagnetic contrast agent in a rat model.

Key words: Monte Carlo modeling; susceptibility contrast; cerebral blood volume mapping; blood oxygenation level-dependent contrast.

INTRODUCTION

A particularly powerful paradigm for functional MR imaging (fMRI) of microvascular hemodynamics incorporates paramagnetic materials that create significant image contrast. These include exogenous (lanthanide chelates) and endogenous (deoxygenated hemoglobin) agents for cerebral blood volume (CBV) mapping and blood oxygenation level-dependent (BOLD) imaging of neuronal activity, respectively. Intravascular compartmentalization of these agents establishes a magnetic susceptibility difference that enhances the transverse relaxation rate ($\Delta R2 = \Delta 1/T_2$) of protons diffusing through the associated intra- and extravascular magnetic field perturbations. This paper summarizes both Monte Carlo model and *in vivo* experiments that elucidate the relationship between microscopic tissue parameters, NMR imaging parameters, and susceptibility contrast *in vivo*. A quantitative understanding of this relationship is required to interpret CBV maps from dynamic first-pass studies using Gd-DTPA (1, 2) and Dy-DTPA (3), as well as BOLD signal changes induced by cerebral neuronal activity associated with task activation (4–7).

This work has three parts. In the first part, we extended previous Monte Carlo simulations of transverse relaxation enhancement (8–13) to generate a more physiological model by including randomly distributed, magnetized cylinders (representing intravascular contrast agent) with an approximation for the contribution from intravascular spins. We predict the dependence of ΔR2 on vessel size as a function of *TE* and pulse sequence (gradient echo (GE), spin echo (SE), and asymmetric spin echo (ASE)), and on vascular volume fraction and susceptibility difference (contrast agent concentration) for a model vasculature with various capillary and non-capillary components. We used a Monte Carlo model to help elicit these relationships for two reasons. First, it is impractical to quantify experimentally the complete dependence of ΔR2 on vessel size and volume fraction, which has been demonstrated in previous studies for spherical (8, 13) and for simple cylindrical (12) magnetic field perturbers. Second, the model helps assess how variation of physiological parameters may influence the concentration dependence of ΔR2 and therefore confound quantitative estimates of fMRI contrast. To this end, we assess the effects of the following on ΔR2* and ΔR2: recruitment-based versus dilation-based increases in volume fraction, distributions of vessel sizes, flowing corpuscles with compartmentalization of contrast agent to the erythrocytes or plasma, and vascular permeability to water.

In the second part, we tested our model by comparing the simulated contrast agent concentration dependence of ΔR2* and ΔR2 with that obtained from serial injection of superparamagnetic contrast agent in a rat model. By simultaneously measuring CBV using a radiolabeled plasma tracer and MR contrast agent concentration, and by using literature values for the vascular size distribution, we eliminated free parameters from the model.

In the third part, we used the validated model to explore aspects of functional imaging that are difficult to discern experimentally. Specifically, we considered the

MRM 34:555–566 (1995)

From the NMR Center, Massachusetts General Hospital, Department of Radiology, and Harvard Medical School (J.L.B., B.R.R., R.M.K.); Center for Imaging and Pharmaceutical Research, Massachusetts General Hospital, Department of Radiology, and Harvard Medical School (L.M.H.); and Harvard-MIT Division of Health Sciences and Technology (J.L.B., B.R.R., R.M.W.), Cambridge, Massachusetts.

Address correspondence to: Jerrold L. Boxerman, MGH NMR Center, Building 149 (2301), 13th Street, Charlestown, MA 02129.

Received December 29, 1994; revised May 10, 1995; accepted June 5, 1995.

This work was supported in part by NIH grants P01 #48729, R01-HL39810, the Whitaker Foundation and a Clement Vaturi Fellowship.

Results presented in this paper were presented at the 1993 SMRM in New York and the 1994 SMR in San Francisco.

0740-3194/95 $3.00

Copyright © 1995 by Williams & Wilkins
All rights of reproduction in any form reserved.

implications of the model for the interpretation of maps of relative CBV (rCBV) and functional activation that are based on microscopic susceptibility changes.

METHODS

Monte Carlo Model

The Monte Carlo methods (14) used here are similar to those that we recently used to quantify ΔR2 for spherical perturbers (13). The differences are summarized below.

1. A proton was placed initially at the origin, and surrounded by randomly oriented cylinders (radius R, susceptibility difference $\Delta\chi$ between the intracylindrical and extracylindrical space). Cylinders filled a volume fraction, f, of a cube with edge $B = 2(A + kR)$, where $A = \sqrt{2\,D\,TE}$ is the expected one-dimensional diffusion distance during the observation time, TE, D is the diffusion coefficient, and $k = 40$ was chosen to minimize boundary effects in the field calculation at the end of each proton's random walk. Larger values of k yielded insignificant differences in estimated ΔR2. For $D = 1 \times 10^{-5}$ cm^2 s^{-1} (typical for cerebral cortex (15, 16) and used throughout this paper) and $TE = 100$ ms, $A \approx 14$ μm, which is significantly less than a typical capillary segment length (≈110 μm (17)), and hence the infinite cylinder model is a reasonable approximation locally. We generated homogeneous spatial distributions of cylinders within Region B by randomly selecting a point and an orientation (uniform longitudinal distribution, co-latitude distributed like $\sin\theta$) for cylinders within a cube with edge $C = 10\ B$. This was repeated until a fraction f of Region B was filled with the volume of overlap accumulated from cylinders intersecting Region B. Region C was chosen to be 10 B because defining cylinders with uniformly distributed points within Region B yields a greater density of cylinders in the center of Region B. Alternatively, random locations and orientations could be chosen from the surface of a sphere.

2. Each proton took 50 steps (Gaussian distributed, $\hat{x}$-, $\hat{y}$- and $\hat{z}$-directed, zero mean, $\sigma = \sqrt{2\,D\,\Delta t}$) per $\Delta TE = 10$ ms (time step $\Delta t = 0.2$ ms). Smaller step sizes yielded insignificant differences in estimated ΔR2 for R between 1 and 100 μm. Because the water exchange rate between the capillary space and tissue in brain is sufficiently slow (exchange times are ≥500 ms (18, 19)), the cylinders were impermeable in initial simulations (typical $TE \leq 100$ ms). Protons beginning a random walk inside (outside) a cylinder therefore stayed inside (outside) that cylinder for the duration of its walk, and proton steps resulting in penetration of cylinders were repeated until a collision-free step was generated. This assumption was relaxed when considering the effect of vascular permeability to water on ΔR2, as described below.

3. The magnetic field perturbation of the external field $B_o\hat{z}$ at each proton position (distance r from the cylinder axis, angle φ with the projection of $B_o\hat{z}$ in a plane orthogonal to the cylinder axis) was evaluated by summing the appropriate intravascular and extravascular $\hat{z}$-directed magnetic field (in cgs units) contributed by each cylinder (at an angle θ with $\hat{z}$) (20):

$$\frac{\Delta B_z(\rho, \varphi)}{B_O} = \begin{cases} 2\pi\,\Delta\chi \left(\frac{R}{r}\right)^2 \cos 2\varphi \sin^2\theta, & r \geq R \\ \frac{2\pi}{3}\,\Delta\chi\,(3\cos^2\theta - 1), & r < R. \end{cases} \quad [1]$$

It was assumed that the fields are noninteracting.

4. The phase accumulated by the nth proton during each step was evaluated by:

$$\Delta\phi_n(t) = \gamma\,\Delta B_z\,\Delta t, \quad [2]$$

and Steps 2–4 were repeated until $t = TE$. SE and GE phases were estimated as described by Weisskoff *et al.* (13). In addition, ASE phases were estimated every 10 ms by combining $\phi_n(t)$ accumulated at 5 ms intervals with appropriate phase inversions. For example, $\phi_n(t)$ for an ASE with $TE = 20$ ms and $\tau = -5$ ms would be $\phi(5\text{ ms}) - [\phi(20\text{ ms}) - \phi(5\text{ ms})] = 2\phi(5\text{ ms}) - \phi(20\text{ ms})$, where τ is the offset of the π-pulse from $TE/2$ (21). Steps 1–4, with re-randomization of all cylinders, were repeated for each of $N_p = 4 \times 10^4$ protons. Larger values of N_p yielded insignificant differences in estimated ΔR2.

5. Finally, estimates for GE, SE, and ASE signal attenuations (S) were computed from $\phi_n(t)$ as described in ref. 13. Associated relaxivity changes were estimated from $-\ln S(TE)/TE$ (22). Although a monoexponential portion of $S(TE)$ can be used to estimate relaxivity change (11), we typically measure signal change in experiments at one TE. Therefore, all references to relaxivity in this paper were estimated from signal attenuations assuming a monoexponential decay of $S(TE)$. An upper bound on the error for the Monte Carlo calculations was computed, and estimates for $\Delta\chi$ between 10^{-8} and 10^{-6} (cgs units) were made from the same set of random walks and perturbers, as described previously (13).

We repeated the entire simulation for R ranging from 1 to 100 μm and f ranging from 1–6%. All simulations were performed on a Silicon Graphics 4D/480/VGX computer.

Modeling Vascular Size Distributions. To compare our model with *in vivo* data, we simulated a simplified vasculature composed of capillaries (radius $R_c = 3$ μm (17)) and macrovessels (radius R_v). We used $R_v = 25$ μm (small venules (23)). As will be shown in Fig. 1, ΔR2*(R) is flat beyond $R = 25$ μm for the $\Delta\chi$s that we consider, and therefore we predict quantitatively similar ΔR2* for vascular models with larger R_v. For ΔR2, there is greater sensitivity to R_v, because ΔR2(R) decreases monotonically for large R. Throughout this paper, we therefore report results for $R_v = 25$ μm and discuss those situations for which significantly different results are obtained for larger R_v. Unless otherwise specified, we assumed equal volume for capillaries and macrovessels, and refer to this balanced vascular model as the "equidistributed" model. This model is based on measured capillary (≈2% (17)) and total (≈4% (24)) volume fractions in cortical gray matter. Total ΔR2 and ΔR2* were estimated by adding ΔR2 and ΔR2*, respectively, for component vessel sizes at appropriate fractions of f. Results from simulations simultaneously including capillaries and macrovessels

did not differ from the combined results from the independent simulations.

Velocity and Compartmentalization of Red Blood Cells. To estimate the effects of red blood cell (RBC) velocity in capillaries, including the restriction of contrast agent to the plasma (exogenous Gd-DTPA) or erythrocytes (endogenous deoxyhemoglobin), we modeled RBCs within a capillary network as an assembly of impenetrable cylinders (R = 3 μm, f = 2%) containing freely permeable spheres (R = 3 μm, Hct = 40%). Each cylinder was placed randomly in space and aligned parallel to the $\hat{x}$, $\hat{y}$, or $\hat{z}$ axis. RBCs were initialized randomly along each vessel. We moved all RBCs and intravascular protons with velocity v, and accumulated the phase of each proton, using the internal and external field descriptions for a magnetized sphere (20) when appropriate. Macrovascular velocity effects were not studied, because macrovessels have a more homogeneous distribution of corpuscles, for which the relaxivity limits to that for a homogeneous cylinder. To estimate BOLD contrast ($\Delta\chi' = 3 \times 10^{-8}$/Hct between the RBC interior and the plasma), phases were computed from the superposed fields from each magnetized sphere. To estimate plasma agent contrast (intravascular agent excluded from the intracellular space), phases were computed by subtracting the superposed field from all magnetized spheres ($\Delta\chi' = 1 \times 10^{-7}/1 - \text{Hct}$) from that due to all uniformly magnetized surrounding cylinders (with the same $\Delta\chi'$). For $v = 0 - 1$ cm/s, we computed $\Delta R2$ and $\Delta R2^*$ from the derived phase distributions as described above.

Vascular Permeability to Water. We accounted for vascular permeability to water (P) by allowing protons colliding with vessel boundaries to traverse the vessel wall with probability p. We solved the equation relating the transport of intravascular and extravascular spins (N_{iv}, N_{ev}) to the permeability-surface area product (PS) and the intravascular and extravascular volumes (V_{iv}, V_{ev}):

$$\frac{dN_{iv}}{dt} = -\frac{PS}{V_{iv}}\left(N_{iv} - \frac{V_{iv}}{V_{ev}}N_{ev}\right) \quad [3]$$

at time TE for the initial condition $N_{ev} = 0$. The fraction of protons initially intravascular that are found in the vessel at time TE (but may have been outside in the interim) is equal to:

$$q = f + (1 - f)e^{-(PS/V)TE}. \quad [4]$$

PS/V is the probability of traversing the vessel per unit time. For physiological $P \approx 1.4 \times 10^{-4}$ cm/s (25) and f = 2%, we expected 91% of the protons to remain intravascular for R = 3 μm and TE = 100 ms.

To obtain an appropriate value for the probability p for a given PS, we used Monte Carlo random walks to estimate q. For each of 4×10^4 random walks for TE = 100 ms, we randomly oriented a volume fraction, f, of R = 3 μm cylinders, and randomly placed a proton inside one cylinder. For each proton step (Δt = 0.2 ms), we allowed protons colliding with cylinder walls to traverse the cylinder wall with probability p. We associated the p yielding q = 0.91 with physiologic P. We compared $\Delta R2(R)$ and $\Delta R2^*(R)$ for the basic model ($P = 0 \Rightarrow p = 0$) with that for varying degrees of P to estimate the effect of vascular permeability to water on $\Delta R2$ and $\Delta R2^*$.

Cumulative Dosing of AMI-227 in Rats

We compared our simulation results with experimental data from cumulative dosing of a long-lived contrast agent in a rat model. Three anesthetized white Wistar rats (318, 272, and 268 g) were imaged on a 4.7 T CSI Omega system (General Electric, Milwaukee, WI) following stepwise injections of a superparamagnetic contrast agent (AMI-227, Advanced Magnetics Inc., Cambridge, MA) with a measured $\Delta\chi$ in blood of 3.4×10^{-7} mM^{-1} at 1.5 T (26). At this field strength, the contrast agent is in the saturable regime (27), and hence the magnetization is the same at 4.7 T. The blood half-life of AMI-227 in rats is greater than 2 h, and hence the blood clearance was minimal during the study. A baseline GE and SE (TR = 1000 ms, TE = 20 ms, 256 × 128 image matrix, 2-mm thick slice, GE flip angle of 45°) image pair was obtained for each rat, followed by six successive injections (2 mg/kg doses of iron) of AMI-227. GE and SE images were acquired after each injection.

Immediately following the imaging protocol, total blood volume (milliliters per 100 g of total body weight) was determined using a radionuclide method. First, a baseline blood sample was drawn. An intravascular tracer, ^{125}I labeled human serum albumin (JENATOPE, Iso-Tex Diagnostics, TX), was then injected intravenously. After allowing the tracer to distribute throughout the intravascular pool, another blood sample was taken. The animal was killed and the brain was immediately removed and frozen in liquid nitrogen. Brain samples corresponding to the imaged slice were obtained. Blood and brain samples were weighed, and the radioactivity in each sample was counted in a gamma counter (Wallac LKB, Turku, Finland) calibrated at 35 keV photopeak. The total blood volume was determined as a tracer dilution volume after correcting the sample gamma counts with their weights. The vascular volume fraction in the brain was determined by normalizing the brain tissue activity with the blood activity.

Image analysis was performed by defining a region of interest (ROI) over the whole brain and computing mean GE and SE signal intensities, from which relaxivity changes were estimated by comparison with the baseline. Vascular contrast agent concentration was computed by assuming uniform distribution of contrast agent in each respective total blood volume. The experimental concentration dependence of $\Delta R2^*$ and $\Delta R2$ was compared with simulation for an equidistributed model (R_v = 25 μm) with f equal to the average cerebral vascular volume fraction, and with f equal to one standard error above and below the average cerebral vascular volume fraction.

RESULTS

Vessel Size Dependence

GE Versus SE Acquisitions. Figure 1 plots $\Delta R2^*(R)$ (TE = 60 ms) and $\Delta R2(R)$ (TE = 100 ms) for f = 2% and $\Delta\chi = 1 \times 10^{-7}$ (corresponding to an intravascular Gd-DTPA concentration of approximately 3.6 mM (26), a typical first-

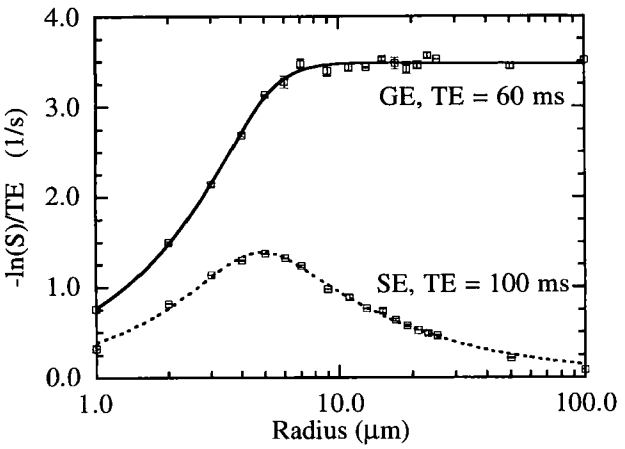

FIG. 1. Size dependence of ΔR2* (*TE* = 60 ms) and ΔR2 (*TE* = 100 ms) for f = 2% and $\Delta\chi = 1 \times 10^{-7}$. At this $\Delta\chi$, ΔR2(R) peaks for microvessels. ΔR2* exceeds ΔR2 at all radii, reaches a plateau for macrovessels, and is actually greater for macrovessels than for microvessels.

pass concentration for a 0.1-mmol/kg injection) at *TE*s typically used for clinical applications at 1.5 T. For this $\Delta\chi$, ΔR2 peaks around R = 5 μm. ΔR2* exceeds ΔR2 at all radii, reaches a plateau for large vessels, and is considerably greater for macrovessels than for microvessels. Weisskoff *et al.* (13) provides an explanation for this size dependence of relaxivity change for the qualitatively similar case of spherical perturbers.

Peak SE Relaxivity. Figure 2 plots ΔR2(R) (f = 2%, *TE* = 100 ms) for $\Delta\chi = 3 \times 10^{-8}$ (corresponding to BOLD contrast with 60% venous oxygenation), 1×10^{-7}, 2×10^{-7} and 4×10^{-7} (corresponding to vascular Gd-DTPA concentrations of 3.6, 7.1, and 14.3 m*M*, respectively). With increasing $\Delta\chi$, ΔR2(R) shifts up and to the left. Over the range of $\Delta\chi$ applicable to endogenous and exogenous contrast-based fMRI, peak ΔR2 is obtained for microvessels (R < 8 μm). Vessels with true mean capillary radii

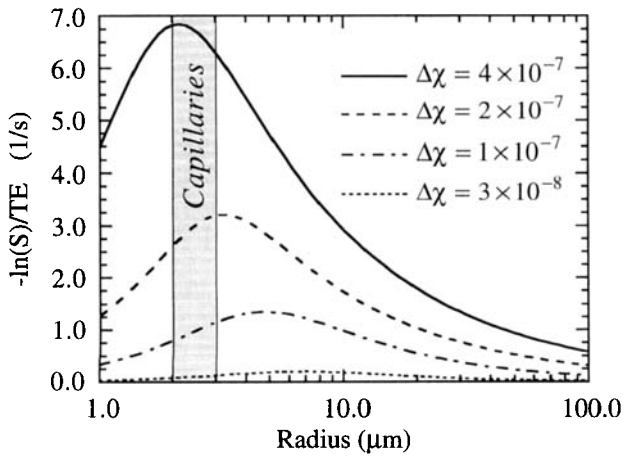

FIG. 2. ΔR2(R) (f = 2%, *TE* = 100 ms) for increasing $\Delta\chi$. Over the range of $\Delta\chi$ applicable to both endogenous and exogenous contrast-based fMRI, peak ΔR2 is obtained for microvessels (R < 8 μm). For $\Delta\chi$ associated with typical first-pass concentrations of Gd-DTPA, peak relaxivity is derived for vessels with true mean capillary radii.

($R \approx$ 2–3 μm) contribute peak ΔR2 for $\Delta\chi$ associated with first-pass concentrations of Gd-DTPA between 7 and 14 m*M*. These results are similar, at least in form, to those generated using spherical perturber models (13).

ASE Acquisitions. For ASE acquisitions, which represent a combination of SE and GE contrast, vascular selectivity is a function of the τ offset. This is demonstrated in Fig. 3, which plots estimated relaxivity change versus R for τ = 0 (SE), +10, +20, +30, and +50 (GE) ms, $\Delta\chi = 3 \times 10^{-8}$ and *TE* = 100 ms. With increasing τ, the size dependence of the relaxivity change becomes more like that for a GE and less like that for a SE.

GE Versus SE CBV Maps. We evaluated how estimates of total and microvascular CBV based on ΔR2* and ΔR2, respectively, varied with vascular composition. Fig. 4 plots ΔR2* (*TE* = 60 ms) versus capillary weighting (α = 0 reflects no capillary contribution, α = 1 reflects no macrovascular contribution) at $\Delta\chi = 1 \times 10^{-7}$ for a vascular model with R_v = 25 μm (weighted by 1 − α) and total f = 4%. At $\Delta\chi = 1 \times 10^{-7}$, ΔR2* decreases by 30% as α increases from 0.1 to 1. Also plotted is ΔR2 (*TE* = 100 ms) versus α for a fixed 2% capillary volume fraction and a macrovascular volume fraction of $2(1/\alpha - 1)$% for R_v = 25 μm. For α > 0.3 (f < 7%), ΔR2 is relatively independent of macrovascular volume fraction.

Volume Fraction Dependence

In Fig. 5, ΔR2* and ΔR2 are plotted against f for $\Delta\chi = 1 \times 10^{-7}$ (Fig. 5a) and $\Delta\chi = 4 \times 10^{-7}$ (Fig. 5b) using both recruitment-based (solid plots) and dilation-based (dashed plots) increases in f for an equidistributed model (R_v = 25 μm) with baseline f = 4%. For recruitment, R_c and R_v were maintained at 3 μm and 25 μm, respectively, but the number of vessels was increased. For dilation, R_c and R_v were increased by the square root of their respective increases in f. Both ΔR2* and ΔR2 are linear with respect to recruitment-based increases in f. While the differences are subtle at these $\Delta\chi$s, there are minor differences with dilatation. At $\Delta\chi = 1 \times 10^{-7}$, dilation-

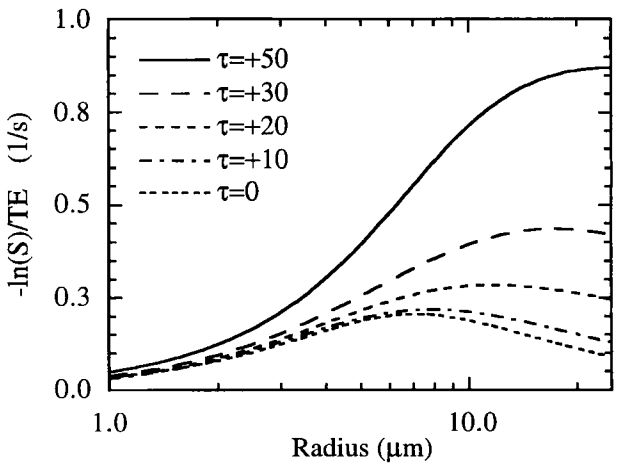

FIG. 3. ASE relaxivity plotted against vessel radius for τ = 0 (SE), +10, +20, +30, and +50 (GE) ms. $\Delta\chi = 3 \times 10^{-8}$ and *TE* = 100 ms. As τ increases from zero, the size dependence of the relaxivity change becomes more like that for GE acquisitions and less like that for SE acquisitions.

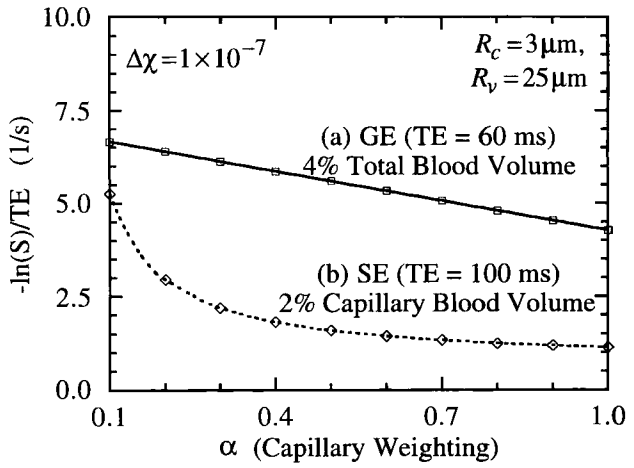

FIG. 4. (a) ΔR2* (*TE* = 60 ms) versus capillary weighting (α = 0 – 1) at $\Delta\chi = 1 \times 10^{-7}$ for a vascular model with R_c = 3 μm (weighted by α) and R_v = 25 μm (weighted by 1 – α) and a total volume fraction of 4%. ΔR2* decreases by 30% as α increases from 0.1 to 1. (b) ΔR2 (*TE* = 100 ms) versus α for a fixed 2% capillary volume fraction and a macrovascular volume fraction of $2(1/\alpha - 1)$% for R_v = 25 μm. For $\alpha > 0.3$ ($f < 7\%$), relaxivity change is relatively independent of the capillary weighting and macrovascular representation.

based ΔR2 tracks recruitment-based ΔR2, but dilation-based ΔR2* slightly exceeds recruitment-based ΔR2*. Conversely, at $\Delta\chi = 4 \times 10^{-7}$, dilation-based ΔR2* tracks recruitment-based ΔR2*, but dilation-based ΔR2 is exceeded by recruitment-based ΔR2. Nonetheless, for both models, ΔR2* and ΔR2 are quite linear over the physiologically relevant range of *f*, suggesting that linearity with *f* is a reasonable assumption regardless of the mechanism of volume increase. For physiologically common changes in *f* between 4 and 6%, the mechanism of volume change influences ΔR2* and ΔR2 by less than 10% at $\Delta\chi = 1 \times 10^{-7}$ and 4×10^{-7}.

Concentration Dependence

Figure 6a plots ΔR2* (*TE* = 60 ms) versus vascular contrast agent concentration (m*M* Gd-DTPA) for a vasculature with total f = 4%, R_c = 3 μm (weighted by α = 0.25, 0.5, and 1) and R_v = 25 μm (weighted by 1 – α). Also plotted is ΔR2 (*TE* = 100 ms) versus Gd-DTPA concentration for a fixed 2% capillary volume fraction and various macrovascular compositions (blood volume of $2(1/\alpha - 1)$%, α = 0.25, 0.5 and 1) with R_v = 25 μm. Figure 6b plots the derivative of the log(relaxivity) versus log(concentration of agent) curve (α = 0.5) and therefore reflects the order of the dependence of relaxivity on contrast agent concentration as a function of concentration. A quadratic increase with Gd-DTPA concentration at low concentrations is observed for both ΔR2* and ΔR2 at all vascular weightings. The GE relationship is generally linear at higher concentrations with little disparity between vascular weightings. By contrast, a more diverse SE profile is obtained over the range of vascular weightings. With increasing capillary weighting for a fixed capillary volume fraction, both ΔR2* and ΔR2 decrease.

TE Dependence

In Fig. 7, ΔR2(*R*) is plotted for *TE* between 20 and 100 ms, f = 2% and $\Delta\chi = 3 \times 10^{-8}$. As *TE* decreases, ΔR2(*R*) shifts down and slightly to the left: both peak ΔR2 and the radius at which the peak occurs decreases.

Velocity and Compartmentalization of Red Blood Cells

Figure 8 depicts the effects of corpuscular flow and restriction of contrast agent to the plasma on ΔR2* (*TE* = 60 ms) and ΔR2 (*TE* = 100 ms) for capillaries. $\Delta\chi' = 1.7 \times 10^{-7}$, corresponding to an average $\Delta\chi = 1.0 \times 10^{-7}$ between the intravascular and extravascular space for Hct = 40%. For typical capillary RBC flow rates of 0.2 cm/s (17), ΔR2* and ΔR2 diminish slightly from that for stationary RBCs, with minimal additional change for $v >$ 0.2 cm/s. Similar results were obtained for BOLD contrast ($\Delta\chi' = 7.5 \times 10^{-8}$, corresponding to an average $\Delta\chi = 3 \times 10^{-8}$ between erythrocytes and plasma). ΔR2* and ΔR2 vary little for changes about physiologic velocities, and hence changes in red cell velocity are not likely to significantly alter estimates of BOLD-based or Gd-based relaxivity change. As v increases, both ΔR2* and ΔR2 plateau at the values predicted using the uniformly magnetized cylinder model (dashed lines) and depicted in Fig. 1, reflecting better averaging of the short-range field perturbations caused by the local compartmentalization.

Vascular Permeability to Water

The effect of permeability is summarized in Fig. 9, which compares ΔR2*(*R*) (*TE* = 60 ms) and ΔR2(*R*) (*TE* = 100 ms) for impermeable vessels (p = 0), physiologic P ($\approx 1.4 \times 10^{-4}$ cm/s, corresponding to $p = 1.5 \times 10^{-3}$) and for freely permeable vessels (p = 1; unrestricted proton diffusion) for f = 2% and $\Delta\chi = 1 \times 10^{-7}$. Maximal P marginally increases ΔR2(*R*) at largest R and decreases ΔR2*(*R*) at small R. For this $\Delta\chi$, these effects are small even for completely unrestricted P, suggesting that differences in P do not significantly affect T_2-weighted, Gd-based estimates of rCBV. Even free permeability (grossly nonphysiologic) does not significantly affect Gd-based ΔR2* or ΔR2 and rCBV estimates, at least in the absence of contrast agent leakage. Virtually identical size dependence curves were obtained for impermeable vessels and physiologic P at BOLD contrast, suggesting that physiologic permeability to water does not significantly impact BOLD relaxivity, either.

Comparison of Model with *in Vivo* Data

A mean total blood volume for the whole rat of 5.8 ml/100 g was measured, and agrees well with the 6 ml/100 g reported by Lee and Blaufox (28). The average measured cerebral blood volume fraction (whole brain) was 1.5% ± 0.4%. Figure 10 plots experimental ΔR2* and ΔR2 against vascular concentration of AMI-227. Because the mass of the rats varied, our constant doses of agent per kg rat yielded different intravascular concentrations after each cumulative injection. Therefore, for each cumulative injection, we obtained means and standard errors for both intravascular concentration and relaxivity from the data for all three rats. Also plotted in

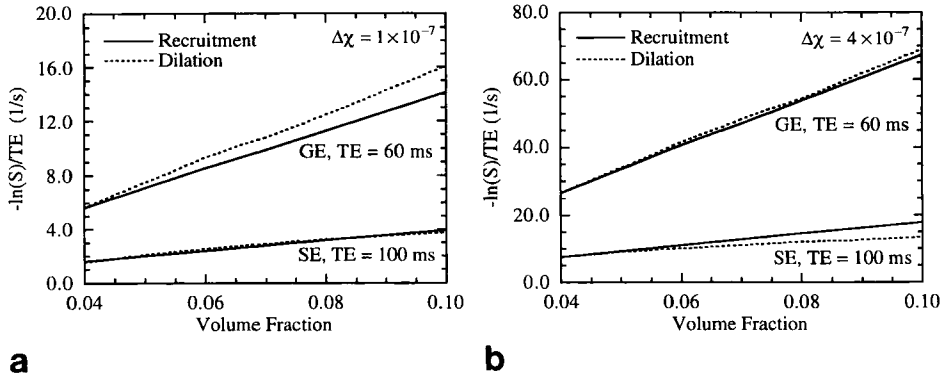

FIG. 5. ΔR2* (*TE* = 60 ms) and ΔR2 (*TE* = 100 ms) versus vascular volume fraction for (a) $\Delta\chi = 1 \times 10^{-7}$ and (b) $\Delta\chi = 4 \times 10^{-7}$ assuming both a recruitment model (solid plots) and a dilation model (dashed plots) for increases in *f* from a baseline of 4% for the equidistributed vascular model with $R_v = 25$ μm. ΔR2* and ΔR2 are linear with respect to recruitment-based increases in *f*. At $\Delta\chi = 1 \times 10^{-7}$, dilation-based ΔR2 tracks recruitment-based ΔR2, but dilation-based ΔR2* slightly exceeds recruitment-based ΔR2*. Conversely, at $\Delta\chi = 4 \times 10^{-7}$, dilation-based ΔR2* tracks recruitment-based ΔR2*, but dilation-based ΔR2 is exceeded by recruitment-based ΔR2. Nonetheless, for both models, ΔR2* and ΔR2 are quite linear over the physiologically relevant range of *f*.

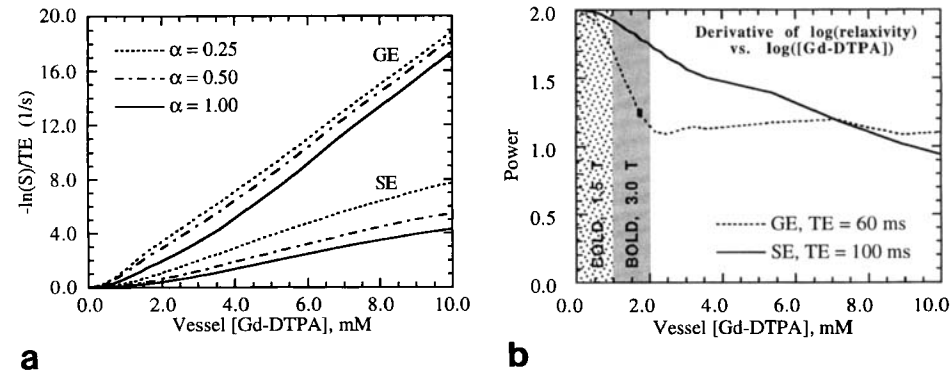

FIG. 6. (a) Dependence of ΔR2* (*TE* = 60 ms) on [Gd-DTPA] for a vasculature with *f* = 4% composed of capillaries (*R* = 3 μm, weighted by α) and venules (*R* = 25 μm, weighted by 1 − α). Also, the dependence of ΔR2 (*TE* = 100 ms) upon [Gd-DTPA] for a fixed 2% capillary volume fraction. (b) Derivative of the log(relaxivity) versus log(concentration of agent) curve (α = 0.5), reflecting the order of the dependence of relaxivity on contrast agent concentration as a function of concentration. A quadratic increase with [Gd-DTPA] at low concentrations is observed at all vascular weightings. ΔR2* is generally linear at higher concentrations with little disparity between vascular weightings. A more diverse SE profile is obtained over the range of vascular weightings.

Fig. 10 are the Monte Carlo ΔR2* and ΔR2 concentration dependence curves for the equidistributed model (R_v = 25 μm) with $f = 1.5\%$ (solid lines) and $f = 1.5\% \pm 0.4\%$ (dashed lines). We found that the experimental data agree with the simulation results to within the standard error of the vascular volume fraction.

DISCUSSION

Monte Carlo Model and *in Vivo* Validation

We have implemented a Monte Carlo model that is more complete than previous Monte Carlo (8–12) and deterministic (29) models of transverse relaxivity change. We now take the opportunity to compare our model results with those of Ogawa *et al.* (11) and Kennan *et al.* (12), and an analytical expression for ΔR2* in the linear gradient regime recently presented by Yablonskiy and Haacke (30). The model of Kennan *et al.* (12) neglected the intravascular contribution to phase, included only vessels orthogonal to the applied field ($\theta = \pi/2$), and included only the magnetic field contribution from the four nearest neighbors (parallel arrangement of vessels with uniform spacing). In Fig. 6a of ref. 12, Kennan *et al.* plot ΔR2* and ΔR2 versus *D* for *R* = 2.5 μm and 7.5 μm, *f* = 5%, and $M = \Delta\chi B_o = 1.6$ mG (corresponding to $\Delta\chi \approx 1 \times 10^{-7}$ at $B_o = 1.5$ T). For $D = 10^{-5}$ cm^2 s^{-1}, Kennan *et al.* predict ΔR2* ≈ 12.5 and 25 s^{-1} at *R* = 2.5 and 7.5 μm, respectively. The corresponding ΔR2 values are approximately 6 and 3 s^{-1}. These values greatly exceed our corresponding estimates (neglecting permeability and flow) of ΔR2* ≈ 4 and 9 s^{-1}, and ΔR2 ≈ 1.8 and 2 s^{-1}. This discrepancy is most likely accounted for by the fact that their simulation only included parallel perturbers on a lattice that were oriented orthogonal to the applied field. Such vessels maximize the field perturbations and do not appropriately represent typical tissue.

Ogawa *et al.* (11) focused exclusively on signal changes due to deoxyhemoglobin and averaged over vessel orientations the signal from a small compartment containing one vessel. Each cylinder was impenetrable, and protons

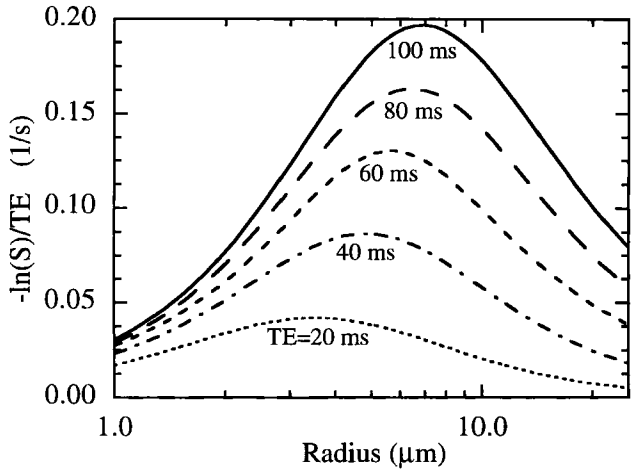

FIG. 7. ΔR2(*R*) for *TE* ranging from 20 to 100 ms. f = 2% and $\Delta\chi = 3 \times 10^{-8}$. As *TE* decreases, the size dependence curve shifts down and to the left: both peak susceptibility change and the radius at which the peak occurs decreases. At lower *TE*, the ratio of relaxivity change for capillary radii (R = 3 μm) to that for venules increases, thereby increasing microvascular selectivity at the cost of overall sensitivity.

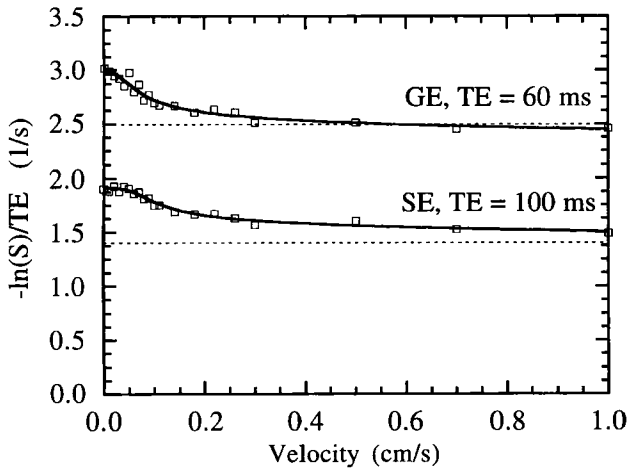

FIG. 8. The effect of corpuscular flow and extracellular restriction of agent on ΔR2* (*TE* = 60 ms) and ΔR2 (*TE* = 100 ms) for R = 3 μm spheres in R = 3 μm vessels. $\Delta\chi' = 1.7 \times 10^{-7}$ between plasma and the extravascular space, corresponding to an average $\Delta\chi = 1.0 \times 10^{-7}$ between the intra- and extravascular space for Hct = 40%. For typical RBC flow rates of 0.2 cm/s, the predicted relaxivity change is slightly less than that for stationary RBCs, and for $v > 0.2$ cm/s, the predicted relaxivity change diminishes minimally. The relaxivities plateau at the values predicted using the uniformly magnetized cylinder model (dashed lines) as v increases.

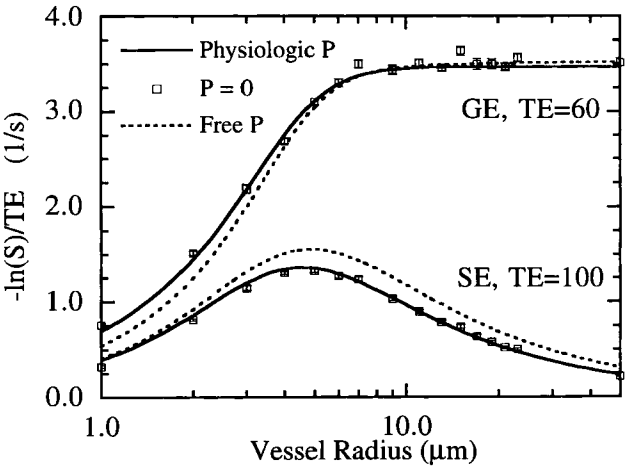

FIG. 9. ΔR2*(*R*) (*TE* = 60 ms) and ΔR2(*R*) (*TE* = 100 ms) for impermeable vessels, freely permeable vessels, and vessels corresponding to physiologic permeability. f = 2% and $\Delta\chi = 1.0 \times 10^{-7}$. Permeability marginally increases ΔR2 for all radii, and decreases ΔR2* relaxivity for microvessels only for very large, unphysiologic permeabilities.

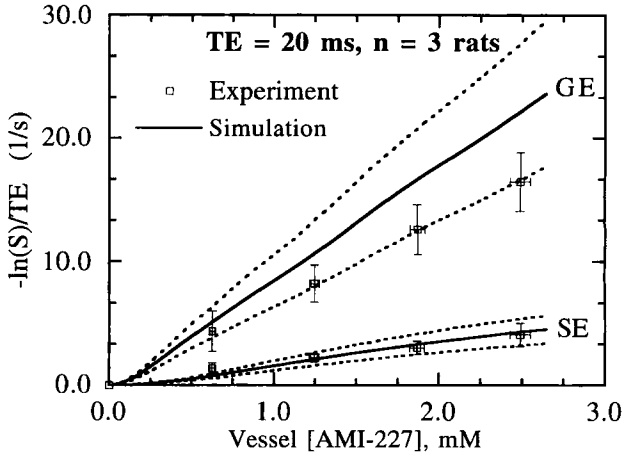

FIG. 10. Comparison of ΔR2* and ΔR2 (*TE* = 20 ms) for simulation (equidistributed model, f = 1.5% (solid lines) and f = 1.5% ± 0.4% (dashed lines), R_v = 25 μm) and experiment as a function of vascular concentration of AMI-227 at 4.7 T. For each cumulative injection, we obtained means and standard errors for both intravascular concentration and relaxivity from the data for all n = 3 rats. The experimental data agree with the simulation results to within the standard error of the vascular volume fraction.

were excluded from the intravascular space. In their notation, $v = \Delta\chi(1 - Y)\omega_o$, where v is the susceptibility-induced frequency shift at the blood vessel surface, $\omega_o = \gamma B_o$, and Y is the oxygen saturation of the blood. For $\Delta\chi$ = 0.1 ppm, Y = 0.7 and B_o = 4 T, v = 32 Hz. In Fig. 4 of Reference (11), ΔR2* plateaus at roughly 2.8 s^{-1} for these parameters and f = 2%. For our simulations at 1.5 T, an equivalent $\Delta\chi$ (equal to $\Delta\chi(1 - Y)$ in the formalism of Ogawa *et al.*) of 8×10^{-8} yields v = 32 Hz. At this $\Delta\chi$, our simulations (neglecting permeability and flow and using their method for computing ΔR2 from signal attenuations at *TE* = 15 ms and *TE* = 40 ms) show that ΔR2* plateaus at approximately 3.2 s^{-1}. The small difference here is most likely due to our inclusion of the intravascular spins.

Equation [22] of the paper by Yablonskiy and Haacke (30) expresses ΔR2* in the linear gradient regime for randomly oriented cylindrical perturbers: $\Delta R2^* = (4\pi/3)f\gamma\Delta M$ (the ΔR2′ in their expression is equivalent to ΔR2* in this regime). For f = 2% and ΔM = 1.5 mG (corresponding to $\Delta\chi = 10^{-7}$ at 1.5 T), they predict

$\Delta R2^* \approx 3.4\ s^{-1}$, which agrees very well with the value of $3.5\ s^{-1}$ that is demonstrated in Fig. 1.

For a given set of biophysical parameters, all models mentioned above solve numerically the same integral over proton phases. The extensions of our model (i.e., the overlapping field contribution from many neighboring vessels) likely generates more physiological phase distributions for comparison with *in vivo* data, particularly in the case of high concentrations of exogenous contrast agent. In addition to methodological differences, none of these other models considered the effects of vascular permeability to water or the flow of red blood cells, but as we have demonstrated, these contributions are relatively small.

Our methodology also differs from previous models by including a portion of the intravascular effect, though not all of it. We account for the decreased T_2' caused by random vessel orientations, but do not account for compartmentalized T_2 effects within the vessels themselves, caused, for example, by deoxygenated red cells. Although this approximation is better than completely ignoring the intravascular effect, it is best suited for Gd-based contrast, for which the 20–50% signal drops are large compared with the vascular volume fraction. The orientation effect is significant. For instance, the analogous $\Delta R2^*(R)$ curve in Fig. 1 obtained from only extravascular spins plateaus at $3\ s^{-1}$ instead of $3.5\ s^{-1}$, and this difference accounts for the discrepancy between our results and those of Ogawa *et al.*

The results depicted in Fig. 10 suggest that excellent agreement with experimental concentration dependence can be obtained with our model using measured values for f and $\Delta\chi$, and with a sensible choice of free model parameters (literature values for vascular distribution). Except for the vascular size distribution, for which literature values were used, there are no free parameters in the model, and hence agreement of simulation and experiment suggest that the model accounts for the majority of signal change in susceptibility contrast MR studies. Agreement between model and experiment does depend, however, on the assumed vascular composition, as suggested by the α-dependence of relaxivity illustrated in Fig. 4. In Fig. 10, predicted $\Delta R2^*$ exceeds experimental $\Delta R2^*$, whereas predicted and experimental $\Delta R2$ are in closer agreement. According to Fig. 4, this suggests that a slightly larger α would fit the data better. The ultimate accuracy of the model therefore depends on the degree to which the vascular composition is known.

Our validated model has utility for exploring aspects of functional imaging that are difficult to determine experimentally. We now consider the implications of the model for (a) the interpretation of CBV mapping, and (b) BOLD functional activation studies. First, the model suggests that the dependence of relaxivity on volume fraction, vessel size, pulse sequence, and contrast agent dose may all impact the interpretation of contrast-based measurement of CBV.

Volume Fraction Dependence

The interpretation of the integral of $\Delta R2(t)$ as rCBV requires that $\Delta R2$ be proportional to volume fraction, f (31). For physiological f, recruitment-based increases in f yield increases in $\Delta R2^*$ and $\Delta R2$ that are proportional to the increase in f. This linear recruitment-based volume fraction dependence is predicted for a vasculature composed of any combination of vessel sizes. Hence the integral of $\Delta R2(t)$ correctly reflects differences in rCBV between regions with recruitment-based changes in volume.

Unlike recruitment-based increases in f, which yield proportional increases in $\Delta R2^*$ and $\Delta R2$ for all radii, changes in R may contribute an additional effect for dilation-based increases in f. Increases in R_v (on the plateau of $\Delta R2^*(R)$ for most $\Delta\chi$, as in Fig. 1) do not increase $\Delta R2^*$ at fixed f. However, microvascular dilation modifies $\Delta R2^*$, increasing it until R_c reaches the plateau of the size dependence curve. In Fig. 5a, a 15% increase in dilation-based $\Delta R2^*$ relative to recruitment-based $\Delta R2^*$ occurs by $f = 10\%$ with respect to the $f = 4\%$ baseline. At $\Delta\chi = 4 \times 10^{-7}$, $R_c = 3\ \mu m$ is on the plateau, and microvascular dilation does not contribute extra $\Delta R2^*$. This accounts for the identical recruitment-based and dilation-based $\Delta R2^*$ curves in Fig. 5b.

Both microvascular and macrovascular dilation can potentially contribute to $\Delta R2$. For modest dilation at $\Delta\chi = 1 \times 10^{-7}$, increased $\Delta R2$ from increased R_c is countered by decreased $\Delta R2$ from increased R_v (radii on opposite sides of the peak $\Delta R2$ in Fig. 2), and the SE dilation curve tracks the SE recruitment curve. For larger increases in f, R_c increases beyond the peak of $\Delta R2(R)$. According to Fig. 1, this transition occurs at an unreasonably large volume fraction (tripling the capillary blood volume), suggesting that for physiological changes in f at $\Delta\chi = 1 \times 10^{-7}$, there should be minimal difference between recruitment-based and dilation-based $\Delta R2$. At $\Delta\chi = 4 \times 10^{-7}$, $R_c = 3\ \mu m$ exceeds the radius at which peak $\Delta R2$ occurs, both microvascular and macrovascular dilation decrease $\Delta R2$, and the SE dilation curve diverges below the SE recruitment curve. This is reflected in Fig. 5b, where a 30% decrease in dilation-based $\Delta R2$ relative to recruitment-based $\Delta R2$ occurs by $f = 10\%$ with respect to the 4% baseline.

Despite these differences, $\Delta R2^*$ and $\Delta R2$ are quite linear for both models and independent of the mechanism of volume increase over the physiologically relevant range of f (4–6%).

Vessel Size Dependence

$\Delta R2(R)$ depicted in Fig. 1 demonstrates the selective microvascular sensitivity of SE acquisitions, and constitutes the appeal of MR for assessing capillary blood volume. Susceptibility-based macrovascular suppression on SE images occurs in addition to that due to nonrefocused spins flowing in large vessels between the $\pi/2$-pulse and π-pulse. SE acquisitions, however, yield significantly reduced signal attenuation, and a trade-off therefore exists between sensitivity and microvascular specificity. Unlike blood flow, which is continuous between vascular segments, we believe that blood volume is likely to be of greatest diagnostic value at the capillary level. Whereas radionuclide techniques that are equally sensitive to all vascular sizes are adequate for measuring flow, they can

only measure total vascular volume, and are therefore less useful in this clinical context. Because even $\Delta R2^*(R)$ is not strictly independent of R, a single susceptibility-based acquisition would appear to be incapable of assessing total vascular volume, unless a high dose of Gd-DTPA or Dy-DTPA were used to push the peak of $\Delta R2^*(R)$ well below capillary sizes. One difficulty with exploiting microvascular-weighted CBV techniques is therefore one of verification, as there appears to be no gold standard against which SE and even GE CBV calculations can be compared.

TE Dependence

The decrease in $\Delta R2$ with decreasing TE shown in Fig. 7 reflects the nonmonoexponential behavior of $S(TE)$. The shift of the peak to smaller radii may be explained qualitatively by considering the range of radii over which relaxivity is expected to demonstrate motional narrowing. This regime exists when two criteria are met: (a) The number of perturbers "sampled" by a proton, $n_s \gg 1$, and (b) $\delta\omega\tau_D \ll 1$, where $\delta\omega$ (proportional to $\Delta\chi$) is the change in Larmor frequency at the surface of a perturber and τ_D is the time required for diffusion past a perturber (32). As TE and the distance traveled by a proton decreases, n_s decreases and a smaller intervessel distance, corresponding to smaller R for fixed f, is required to enforce Criterion (a). Hence the peak of $\Delta R2(R)$, which signifies the transition from the motionally narrowed regime, occurs at smaller R. As $\Delta\chi$ decreases, this shift becomes relatively more prominent, as is seen by considering the effects of $\Delta\chi$ at long and short TE. At long TE, Criterion (a) is met, and the peak radius is influenced more sensitively by $\Delta\chi$. With increasing $\Delta\chi$, the motionally narrowed regime is preserved with decreasing τ_D (proportional to R^2), which accounts for the left shift of $\Delta R2(R)$ with increasing $\Delta\chi$. On the other hand, at short TE, position of the peak is more sensitive to Criterion (a), and relatively insensitive to $\Delta\chi$. Therefore, in BOLD studies for which $\Delta\chi$ is almost an order of magnitude smaller than that for exogenous contrast acquisitions, a more prominent relative left shift occurs with decreasing TE. It is therefore important to note that TE, in addition to $\delta\omega\tau_D$, is an important factor that determines the relaxivity characteristics of the system.

One significance of the shift in peak $\Delta R2$ with TE is that at lower TE, the ratio of capillary $\Delta R2$ to that for macrovessels increases, thereby increasing microvascular selectivity at the cost of overall sensitivity. For example, in Fig. 7, the ratio of $\Delta R2(R = 3\ \mu m)$ to $\Delta R2(R = 25\ \mu m) \approx 8$ at $TE = 20$ ms and $\Delta\chi = 3 \times 10^{-8}$, but only ≈ 1.5 at $TE = 100$ ms, and so SE acquisitions at $TE = 20$ ms would be expected to offer greater microvascular selectivity. However, this additional specificity comes at a great cost of sensitivity, by a factor of roughly 4. As a result, this selectivity may have more theoretical than practical significance.

GE Versus SE CBV Maps

Curve (a) of Fig. 4 suggests that even though $\Delta R2^*(R)$ is not strictly independent of R, GE acquisitions may be used to approximately reflect total CBV changes, because $\Delta R2^*$ for vascular models with fixed total f is relatively independent of the capillary weighting (α). This implies that for a given tracer concentration, a measured value of $\Delta R2^*$ reflects a relatively unique f, regardless of the vascular composition. We find a 30% difference in $\Delta R2^*$ between the $\alpha = 0$ and $\alpha = 1$ models at $\Delta\chi = 1 \times 10^{-7}$ (compared with a 10% difference at $\Delta\chi = 4 \times 10^{-7}$). The discrepancy is smaller at larger $\Delta\chi$ because R_c is on the plateau of the size dependence curve, and hence changes in α do not affect changes in total $\Delta R2^*$. At low $\Delta\chi$, $\Delta R2^*$ is more sensitive to α, because R_c has not reached the plateau and differences in relaxivity (and CBV estimates) may therefore either reflect true differences in f for similar vascular compositions, or different compositions with the same f. This latter case presents a caution for proper interpretation of CBV maps, because CBV ratios between two regions are dependent on differences in vascular composition.

Similarly, Curve (b) of Fig. 4 suggests that SE acquisitions approximately reflect microvascular CBV changes, because $\Delta R2$ for vascular models with fixed capillary f is relatively independent of the capillary weighting and macrovascular representation for $\alpha > 0.3$. As R_v increases, the discrepancy between $\Delta R2$ for the $\alpha = 0.3$ and $\alpha = 1$ models decreases, because $\Delta R2$ decreases with increased R_v, and hence the relative macrovascular contribution is less for models with large R_v. These results, combined with the recruitment versus dilation results, suggest that GE and SE comparisons of total and microvascular rCBV, respectively, can be made, and that the error decreases with increasing $\Delta\chi$. This simplified interpretation (i.e., $\Delta R2^*$ reflects total blood volume and $\Delta R2$ reflects capillary blood volume) motivated the presentation style of Figs. 4 and 6a.

With these effects in mind, it seems reasonable that a 30% difference in rCBV values is not likely to be attributed to physiological variability of non-blood volume parameters (representing false positives). Similarly, a 30% difference in rCBV values is not likely to be erased by physiological variability of non-blood volume parameters (representing false negatives). Differences in rCBV values much smaller than 30% may not reflect true differences in blood volume, and should be considered with caution when staging neoplasms, etc. For example, if $\alpha = 0.5$ for normal brain, then 30% differences in rCBV could be attributed to variations in α (from 0.3–1.0), D (from $0.5–2.0 \times 10^{-5}$ cm/s), or to a wide range of permeability and blood cell velocities.

Contrast Agent Dose

Figure 2 illustrates the advantages of increasing the dose of contrast agent. For $\Delta\chi$ increasing from 1×10^{-7} to 2×10^{-7} to 4×10^{-7} (approximately corresponding to Gd-DTPA doses of 0.1, 0.2, and 0.4 mg/kg), two beneficial changes occur. First, the absolute level of relaxivity increases for all radii, thereby providing greater rCBV SNR. Second, the relaxivity size dependence curves shift up and to the left, providing greater microvascular selectivity for SE acquisitions. An explanation for the shift with increasing $\Delta\chi$ is provided by Weisskoff *et al.* (13) using scaling laws derived from the Bloch-Torrey equation.

While volume fraction, vessel size dependence, pulse sequence, and contrast agent dose may impact our inter-

pretation of CBV maps, our model also suggests that flow, vascular permeability and nonlinearities of the concentration dependence of relaxivity are relatively unimportant for correct interpretation of contrast-based measurement of CBV.

Compartmentalization and Corpuscular Flow

The small decrease in relaxivity with increased velocity is explained qualitatively by assuming that motion of RBCs acts like an increase in diffusion to an extravascular proton, which corresponds to a left shift on the x-axis of Fig. 1 which scales like R^2/D (13). Increased D therefore decreases microvascular $\Delta R2^*$ (including $R = 3$ μm). For SE acquisitions with $\Delta\chi \leq 5 \times 10^{-7}$ (see Fig. 2), microvascular $\Delta R2$ should decrease. Only for exceptionally large $\Delta\chi$ will these flow rates serve to increase microvascular $\Delta R2$, and this behavior forms the basis for the technique proposed by Hardy *et al.* for measuring flow (9). Even for capillaries, which are on the steep part of the size-dependence curve for typical $\Delta\chi$s, the change in relaxivity is rather small, and hence this effect is not likely to significantly alter predicted relaxivity change and estimates of CBV. For $v \geq 0.2$ cm/s, the predicted relaxivity change diminishes minimally. As v increases, $\Delta R2^*$ and $\Delta R2$ approach the values predicted using the homogeneous cylinder model (dashed lines in Fig. 8). This reflects better averaging of the compartment-based extravascular field perturbations. There is very little difference between predicted relaxivity change using the homogeneous cylinder model and the extracellular compartment model with $v \geq 0.2$ cm/s (typical RBC velocity in capillaries). Therefore, the homogeneous cylinder model should not significantly underestimate relaxivity change by ignoring these effects.

Vascular Permeability to Water

Figure 9 demonstrates that the susceptibility-induced change in T_2 is unaffected by permeability, even for extreme values of P. P values within a physiologic range virtually do not affect Gd-based $\Delta R2^*$ or $\Delta R2$ and hence rCBV estimates. By considering free permeability, which corresponds to a nonphysiologic permeability far greater than that for even highly pathologic cases, we determined that even gross disruption of the blood-brain barrier would not significantly impact susceptibility-induced relaxivity change. While our calculation neglected dipole-dipole relaxation, which might affect T_2 in nonphysiological ($p = 1$) cases, such an effect can be neglected for permeabilities typical of the most water permeable membranes, for which $P \approx 10^{-2}$ cm/s. This analysis also ignores the associated T_1 effects, which for Gd-DTPA would increase with increased water permeability (more protons enter the coordination sphere of a Gd-DTPA molecule) and also with increased leakage of agent.

Concentration Dependence

For GE acquisitions, Fig. 6 depicts a quadratic concentration dependence at small $\Delta\chi$, which decreases to a linear dependence at large $\Delta\chi$ for all vascular compositions. The transition from quadratic to linear regime occurs at a larger $\Delta\chi$ with increasing microvascular composition. As R increases, the range of $\Delta\chi$ over which superlinear behavior exists shrinks, so that for purely large macrovascular compositions, there is nearly no superlinear regime. The family of GE concentration dependence curves for different vascular compositions are parallel with linear dependence at sufficiently large $\Delta\chi$ because eventually all vascular components are on the plateau of $\Delta R2^*(R)$. On the plateau of the size-dependence curve, increases in $\Delta\chi$ yield linear increases in relaxivity, because there is no additional size effect from perturbers that are larger (13).

For SE acquisitions, a superlinear regime exists for all vascular compositions at sufficiently low $\Delta\chi$ for which all vessel sizes are to the left of the peak radius for $\Delta R2(R)$ and for which relaxivity increases like R^2. This region corresponds to the motionally narrowed regime previously described by the models of Gillis and Koenig (32). The $\Delta\chi$ for which this is true is smaller for macrovessels than for microvessels, and hence the macrovascular compositions exit the superlinear regime at a lower $\Delta\chi$. As $\Delta\chi$ gets sufficiently large and the microvascular radii pass the peak radii, there is sublinear increase with $\Delta\chi$. This sublinear regime is expected to occur sooner for macrovascular-weighted compositions than for microvascular-weighted compositions, and this behavior is observed in Fig. 6.

Despite this nonlinear dependence of relaxivity on contrast agent concentration, relative CBV maps constructed from common input boluses should properly reflect relative differences in CBV. While classical tracer kinetics describes the method for computing blood volume from a concentration-time curve (31), this method is only valid when the signal can be converted into an average tissue concentration. For an intravascular agent, this would require linearity in both vessel volume fraction and concentration of agent within the vessel. However, in certain cases, the formalism remains valid as long as the signal is proportional to blood volume regardless of the concentration dependence. One such case is when the primary cause of tracer dispersion is morphometrical heterogeneity rather than diffusion within the plasma.

We can see this by considering each vessel to be a chain of subvessels, and assuming that the proton diffusion lengths are short compared with the gradients of contrast agent concentration along the vessel. For vascular segments of 110 μm (17) and a RBC velocity of 0.2 cm/s, the transit time per segment is roughly 0.1 s, which is short compared with the variations in bolus concentration as reflected by the 5 s typically required for peak signal attenuation during bolus passage. Let $G\{c\}$ denote the intravascular concentration dependence of $\Delta R2$, given by the infinite cylinder model. Then $\Delta R2$ at any moment in time can be estimated by adding the appropriately weighted $\Delta R2$ contributed by every subvessel. Integrating over time, exchanging the order of integration and summation, and recognizing the independence of the integral to any offset in time, we find:

$$\Delta R2(t) = \sum_{i=1}^{N_v} \sum_{j=1}^{N_c} \frac{V_i}{N_c} \cdot G\{c_j(t)\}, \qquad [5]$$

where N_v is the number of vessels, $N_c = V_i/F_i\Delta t$ is the number of straight segment subvessels in the ith vessel, and $c_j(t) = c_{in}(t - j\Delta t)$is the delayed input concentration in the jth cell of the ith vessel. Integrating $\Delta R2(t)$ over time yields:

$$\int_0^\infty dt\, \Delta R2(t) = V \int_0^\infty dt\, G\{c_{in}(t)\}, \qquad [6]$$

and hence the area under the $\Delta R2(t)$ curve equals the CBV scaled by the area under the input concentration operated on by $G\{*\}$. This is true regardless of the nature of $G\{*\}$. Therefore, relative CBV maps constructed from common input boluses should properly reflect relative differences in CBV. Comparison of maps generated using different contrast agent injections may not satisfy this property, because even if the anatomy, $G\{*\}$, and $\int dtc_{in}(t)$ are the same, $c_{in}(t)$ is likely to differ from injection to injection.

Some aspects of the model pertain specifically to BOLD assessment of functional activation, for which low $\Delta\chi$ and a desire to maintain microvascular selectivity (presumably a better reflection of localized neuronal activation) are the distinguishing features. One limitation of the application of this model to BOLD fMRI is that it omits the corpuscular nature of the compartmentalized T_2 effect, for the intravascular spins contribute the majority of fMRI signal change at 1.5 T (33). However, we can still comment on the extravascular signal changes that would likely predominate for either high field strengths at which the relative contribution of the intravascular spins is less substantial, or for techniques that eliminate the intravascular spins (33).

Vessel Size Dependence

The trade-off between sensitivity (GE) and microvascular specificity (SE) is more important for BOLD rather than Gd-based acquisitions, because the contrast is inherently smaller. As suggested by Fig. 3, the τ offset of ASE acquisitions might lend a degree of freedom with which a compromise between signal sensitivity and microvascular selectivity can be made. The efficacy of ASE acquisitions for functional imaging was recently demonstrated by Baker *et al.* (34).

Concentration Dependence

Figure 6b suggests that in the low $\Delta\chi$ regime that corresponds to venous and capillary oxygenation, relaxivity depends superlinearly (although not fully quadratically) on $\Delta\chi$. Note that for 2 m*M* Gd-DTPA, which corresponds to BOLD contrast due to 60% oxygenation at 3 T, the concentration dependence of $\Delta R2^*$ is close to linear. Because it is the product of $\Delta\chi$ and field strength that determines relaxivity, these results, which include some of the intravascular contribution, predict that BOLD GE relaxivity should not demonstrate anywhere near a quadratic field strength dependence, and if superlinear at all, should be close to linear. In addition, because the relative contribution of intravascular spins decreases with increasing field, it is not surprising that recent studies have reported a field strength dependence for BOLD contrast that is close to linear (35). The field strength dependence is particularly significant for SE acquisitions. Although they offer nearly inadequate sensitivity at 1.5 T, we predict SE acquisitions will be increasingly viable at higher fields. Finally, Fig. 2 demonstrates that $\Delta R2(R)$ for BOLD contrast is shifted down and to the right compared with $\Delta R2(R)$ for the higher $\Delta\chi$s in contrast agent injections. Therefore, BOLD contrast confers less inherent microvascular specificity than Gd-based contrast, even for SE acquisitions.

CONCLUSIONS

We developed a Monte Carlo model with which we quantified the relationship between morphometrical (vessel size, vascular volume fraction), biophysical (vascular permeability to water, flow of red blood cells), and experimental (contrast agent concentration, *TE*) parameters and susceptibility contrast *in vivo*. We found vascular permeability to water and the flow of erythrocytes to be relatively unimportant contributors to susceptibility-based $\Delta R2$. However, pulse sequence, *TE*, and concentration of contrast agent have profound effects on the vessel size dependence of $\Delta R2$. For a model vasculature containing capillaries and venules, we predicted a linear volume fraction dependence for physiological volume changes based on recruitment and dilation mechanisms, and a concentration dependence that is nonlinear and pulse sequence-dependent. Using the model, we showed that spin echo functional images have greater microvascular sensitivity than gradient echo images, and that the specifics of the volume fraction and concentration dependence of relaxivity should allow for robust mapping of relative blood volume. We also demonstrated excellent agreement between the predictions of our model and experimental data obtained from serial injection of superparamagnetic contrast agent in a rat model. Because of the strong size dependence of relaxivity change, and the inherent difficulty of measuring the complete vascular size dependence, validation of the model with no free parameters remains a challenge. However, our model also suggests the potential for elucidating greater information about vascular morphometry by varying *TE*, $\Delta\chi$, and pulse sequence, and making qualitative and quantitative assessments about the underlying physiology.

REFERENCES

1. B. Rosen, J. Belliveau, H. Aronen, D. Kennedy, B. Buchbinder, A. Fischman, M. Gruber, J. Glas, R. Weisskoff, M. Cohen, F. Hochberg, T. Brady, Susceptibility contrast imaging of cerebral blood volume: human experience. *Magn. Reson. Med.* **22,** 293–299 (1991).
2. S. Warach, W. Li, M. Ronthal, R. Edelman, Acute cerebral ischemia: evaluation with dynamic contrast-enhanced MR imaging and MR angiography. *Radiology.* **182,** 41–47 (1992).
3. A. Sorensen, S. Kulke, R. Weisskoff, J. Boxerman, B. Buchbinder, B. Rosen, *in* "American Society of Neuroradiology Annual Meeting, Nashville, 1994," p. 237.
4. K. Kwong, J. Belliveau, D. Chesler, I. Goldberg, R. Weisskoff, B. Poncelet, D. Kennedy, B. Hoppel, M. Cohen, R. Turner, H.

Cheng, T. Brady, B. Rosen, Dynamic magnetic resonance imaging of human brain activity during primary sensory stimulation. *Proc. Natl. Acad. Sci. (USA)* **89,** 5675–5679 (1992).
5. P. Bandettini, E. Wong, R. Hinks, R. Tikofsky, J. Hyde, Time course EPI of human brain function during task activation. *Magn. Reson. Med.* **25,** 390–397 (1992).
6. S. Ogawa, D. Tank, R. Menon, J. Ellermann, S. Kim, H. Merkel, K. Ugurbil, Intrinsic signal changes accompanying sensory stimulation: Functional brain mapping with magnetic resonance imaging. *Proc. Natl. Acad. Sci. (USA)* **89,** 5951–5955 (1992).
7. R. Turner, P. Jessard, H. Wen, K. Kwong, D. Le Bihan, T. Zeffiro, R. Balaban, Mapping of the human visual cortex at 4 and 1.5 T using deoxygenation contrast EPI. *Magn. Reson. Med.* **29,** 277–279 (1993).
8. C. Fisel, J. Ackerman, R. Buxton, L. Garrido, J. Belliveau, B. Rosen, T. Brady, MR contrast due to microscopically heterogeneous magnetic susceptibility: numerical simulations and applications to cerebral physiology. *Magn. Reson. Med.* **17,** 336–347 (1991).
9. P. Hardy, R. Henkelman, On the transverse rate enhancement induced by diffusion of spins through inhomogeneous fields. *Magn. Reson. Med.* **17,** 348–356 (1991).
10. R. Muller, P. Gillis, F. Moiny, A. Roch, Transverse relaxivity of particulate MRI contrast media: from theories to experiments. *Magn. Reson. Med.* **22,** 178–182 (1991).
11. S. Ogawa, R. Menon, D. Tank, S. Kim, H. Merkle, J. Ellermann, K. Ugurbil, Functional brain mapping by blood oxygenation level-dependent contrast magnetic resonance imaging: a comparison of signal characteristics with a biophysical model. *Biophys. J.* **64,** 803–812 (1993).
12. R. Kennan, J. Zhong, J. Gore, Intravascular susceptibility contrast mechanisms in tissues. *Mag. Reson. Med.* **31,** 9–21 (1994).
13. R. Weisskoff, C. Zuo, J. Boxerman, B. Rosen, Microscopic susceptibility variation and transverse relaxation: theory and experiment. *Magn. Reson. Med.* **31,** 601–610 (1994).
14. M. Kalos, P. Whitlock, "Monte Carlo Methods," John Wiley & Sons, Inc., New York, 1986.
15. D. Chien, R. Buxton, K. Kwong, B. Rosen, MR diffusion imaging of the human brain. *J. Comput. Assist. Tomogr.* **14,** 514–520 (1990).
16. A. Bizzi, A. Righini, R. Turner, D. LeBihan, D. DesPres, G. Di Chiro, J. Alger, MR of diffusion slowing in global cerebral ischemia. *Am. J. Neuroradiol.* **14,** 1347–1354 (1993).
17. G. Pawlik, A. Rackl, R. Bing, Quantitative capillary topography and blood flow in the cerebral cortex of cats: an *in vivo* microscopic study. *Brain Res.* **208,** 35–58 (1981).
18. J. Eichling, M. Raichle, R. Grubb, M. Ter-Pogossian, Evidence of the limitations of water as a freely diffusible tracer in brain of the rhesus monkey. *Circ. Res.* **35,** 358–364 (1974).
19. O. Paulson, M. Hertz, T. Bolwig, N. Lassen, Filtration and diffusion of water across the blood-brain barrier in man. *Microvasc. Res.* **13,** 113–124 (1977).
20. S. Chu, Y. Xu, J. Balschi, C. Springer, Bulk magnetic susceptibility shifts in NMR studies of compartmentalized samples: use of paramagnetic reagents. *Magn. Reson. Med.* **13,** 239–262 (1990).
21. B. Hoppel, R. Weisskoff, K. Thulborn, J. Moore, K. Kwong, B. Rosen, Measurement of regional blood oxygenation and cerebral hemodynamics. *Magn. Reson. Med.* **30,** 715–723 (1993).
22. J. Belliveau, B. Rosen, H. Kantor, R. Rzedzian, D. Kennedy, R. McKinstry, J. Vevea, M. Cohen, I. Pykett, T. Brady, Functional cerebral imaging by susceptibility-contrast NMR. *Magn. Reson. Med.* **14,** 538–46 (1990).
23. C. Caro, T. Pedley, R. Schroter, W. Seed, "The Mechanics of the Circulation," Oxford University Press, New York, 1978.
24. K. Leenders, D. Perani, A. Lammertsma, J. Heather, P. Buckingham, M. Healy, J. Gibbs, R. Wise, J. Hatazawa, S. Herold, R. Beaney, D. Brooks, T. Spinks, C. Rhodes, R. Frackowiak, T. Jones, Cerebral blood flow, blood volume and oxygen utilization: normal values and effect of age. *Brain* **113,** 27–47 (1990).
25. M. Neuder, B. Jenkins, D. Chesler, J. Moore, R. Lauffer, B. Rosen, *in* "Proc., SMRM, 10th Annual Meeting, San Francisco, 1991," p. 707.
26. R. Weisskoff, S. Kiihne, MRI susceptometry: image-based measurement of absolute susceptibility of MR contrast agents and human blood. *Magn. Reson. Med.* **24,** 375–383 (1992).
27. L. Josephson, J. Bigler, D. White, The magnetic properties of some materials affecting MR images. *Magn. Reson. Med.* **22,** 204–208 (1991).
28. H. Lee, M. Blaufox, Blood volume in the rat. *J. Nucl. Med.* **26,** 72–76 (1985).
29. E. Wong, P. Bandettini, *in* "Proc., SMRM, 12th Annual Meeting, New York, 1993," p. 10.
30. D. Yablonskiy, E. Haacke, Theory of NMR signal behavior in magnetically inhomogeneous tissues: the static dephasing regime. *Magn. Reson. Med.* **32,** 749–763 (1994).
31. R. Weisskoff, D. Chesler, J. Boxerman, B. Rosen, Pitfalls in MR measurement of tissue blood flow with intravascular tracers: which mean transit time? *Magn. Reson. Med.* **29,** 553–558 (1993).
32. P. Gillis, S. Koenig, Transverse relaxation of solvent protons induced by magnetized spheres: application to ferritin, erythrocytes, and magnetite. *Magn. Reson. Med.* **5,** 323–345 (1987).
33. J. Boxerman, P. Bandettini, K. Kwong, J. Baker, T. Davis, B. Rosen, R. Weisskoff, The intravascular contribution to fMRI signal change: Monte Carlo modeling and diffusion-weighted studies *in vivo*. *Magn. Reson. Med.*, **34,** 4–10 (1995).
34. J. Baker, B. Hoppel, C. Stern, K. Kwong, R. Weisskoff, B. Rosen, *in* "Proc., SMRM, 12th Annual Meeting, New York, 1993," p. 1400.
35. P. Bandettini, E. Wong, A. Jesmanowicz, R. Prost, R. Cox, R. Hinks, J. Hyde, *in* "Proc., SMR, 2nd Annual Meeting, San Francisco, 1994," p. 434.